2/9/11/78

PREPRINT UCRL-80211

CONF-780824--5

Lawrence Livermore Laboratory

Speckle Imaging Using The Principle Value Decomposition Method

James W. Sherman

August 25, 1978

SPIE Tech. Symposium '78, San Diego, 8/28-8/31

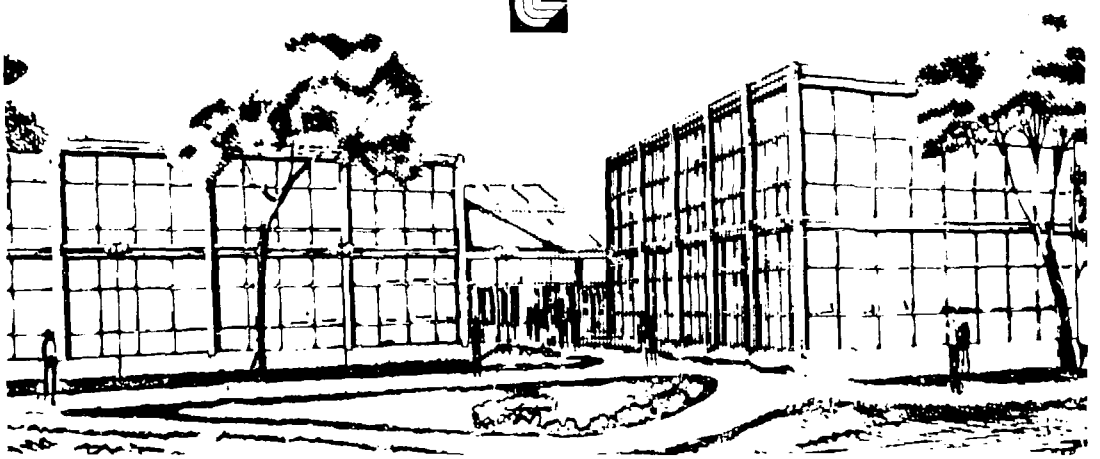

149-09

SPECKLE IMAGING USING THE PRINCIPLE VALUE DECOMPOSITION METHOD*

James W. Sherman
Lawrence Livermore Laboratory, University of California
Livermore, California 94550

Abstract

Obtaining diffraction limited images in the presence of atmospheric turbulence is a topic of current interest. Two types of approaches have evolved: real-time correction and speckle imaging. Using an "optimal" filtering approach, we have developed a speckle imaging restoration method. This method is based on a non-linear integral equation which is solved using principle value decomposition.

The method has been implemented on the CDC 7600 for study. The restoration algorithm is discussed and it's performance is illustrated.

Introduction

In recent years, there has been considerable interest in the removal of atmospheric turbulence effects from telescopic imagery. The effects of atmospheric turbulence on optical propagation are random and vary both spatially and temporally, and for photographs taken under a variety of conditions, the random process characterizing the turbulence can be considered spatially and temporally stationary. If the exposure times are sufficiently short (1/100 sec.), the atmosphere can be effectively frozen. Then a number of images of the same object can be used to estimate a restored image of the object.

This paper describes the continuation of our efforts previously reported [1]. The principle value decomposition method uses the coherence obtained with second order statistics. Labeyrie [2] averaged the modulus of speckle images to obtain the spectrum and autocorrelation of images. This speckle interferometry has been used to measure the separation of binary stars. Knox and Thompson [3] developed an ad hoc method which estimates the phase information needed to recover an image from the second order statistics. Several others [4,5,6,7,8] have considered the recovery of image information using these types of methods.

The emphasis of this paper is on the application of "optimal" filtering approaches to this problem. First, the speckle imaging model and the first and second order statistics of speckle images will be briefly reviewed. Then the restoration algorithm based upon principle value decomposition will be presented and discussed. Finally, the performance will be illustrated by real and simulated restorations.

Speckle Image Model

Two principal sources of image distortion occur when using a ground-based telescope. The first is the turbulence of the intervening atmosphere. The second source is the error or noise associated with the physical measurement of the image. Both mechanisms adversely affect the quality of the imaging and mask many of the important features of the object. While the turbulence effects are the most profound in this regard, it is the presence of the noise which has previously made correction for the turbulence difficult. Models for both effects will be described next.

Model for the Turbulence Effects

For simplicity, consider incoherent imaging over an isoplanatic patch, the image can be expressed as a convolution of the object and a point spread response function:

$$i_f(\underline{x},t) = \int_{-\infty}^{\infty}\int o(\underline{\lambda})s(\underline{x} - \underline{\lambda}, t)d\underline{\lambda} \qquad (1)$$

where $i_f(\underline{x},t)$ is the formed image, $o(\underline{\lambda})$ is the object, and $s(\underline{x},t)$ is the point spread response. The point spread response depends on the optical system and the phase delay and amplitude disturbance processes caused by turbulence. Let $S(\underline{z},t)$ be the optical transfer function corresponding to $s(\underline{x},t)$, that is,

*This work was performed under the auspices of the U.S. Department of Energy under Contract Number W-7405-ENG-48.

$$S(\underline{z},t) = \mathcal{F}_{\underline{x}}\{s(\underline{x},t)\} = \iint_{-\infty}^{\infty} a(\underline{\rho}+\underline{z})\,a(\underline{\rho}) \exp\{j\phi(\underline{\rho}+\underline{z}) - j\phi(\underline{\rho})\}$$

$$\exp\{\psi(\underline{\rho}+\underline{z},t) - j\beta(\underline{\rho}+\underline{z},t) + \psi(\underline{\rho},t) - j\beta(\underline{\rho},t)\}\, d\underline{\rho} \qquad (2)$$

$a(\cdot)$ is the aperture function of the telescope,

$\phi(\cdot)$ is the phase aberration function of the telescope,

$\psi(\cdot,\cdot)$ is the log-amplitude disturbance at the aperature caused by turbulence,

$\beta(\cdot,\cdot)$ is the phase delay disturbance at the aperture caused by turbulence,

and $\mathcal{F}_{\underline{x}}\{\cdot\}$ indicates Fourier transform with respect to x.

Assuming the usual Gaussian distribution for ψ and β allows the mean and covariance of $S(\underline{z},t)$ to be written in terms of the wave structure function, $D(\cdot)$. Using the results of Fante [5], the mean and covariance of $S(\underline{z},t)$ are well approximated by

$$\bar{S}(\underline{z}) = \exp\{-\tfrac{1}{2} D(\underline{z})\} \iint_{-\infty}^{\infty} a(\underline{\rho}+\underline{z})a(\underline{\rho}) \exp\{j\phi(\underline{\rho}+\underline{z}) - j\phi(\underline{\rho})\}\, d\underline{\rho} \qquad (3)$$

and

$$S_s(\underline{z}_1,\underline{z}_2) = \iiint_{-\infty}^{\infty} a(\underline{\rho}_1+\underline{z}_1)a(\underline{\rho}_1)a(\underline{\rho}_2+\underline{z}_2)a(\underline{\rho}_2)\exp\{j\phi(\underline{\rho}_1+\underline{z}_1) - j\phi(\underline{\rho}_1) + j\phi(\underline{\rho}_2+\underline{z}_2) - j\phi(\underline{\rho}_2)\} \qquad (4)$$

$$\exp\left[-\frac{D(\underline{z}_1)+D(\underline{z}_2)}{2}\right]\left[\exp\left[-\frac{D(\underline{\rho}_1-\underline{\rho}_2+\underline{z}_2)+D(\underline{\rho}_1-\underline{\rho}_2-\underline{z}_2)-D(\underline{\rho}_1-\underline{\rho}_2)-D(\underline{\rho}_1-\underline{\rho}_2+\underline{z}_1-\underline{z}_2)}{2}\right]-1\right] d\underline{\rho}_1, d\underline{\rho}_2$$

For mean $S(\underline{z})$ the effects of the atmosphere and the telescope separate into a product form, but for the covariance $S_s(\underline{z}_1,\underline{z}_2)$, they do not. $\bar{S}(\underline{z})$ is dominated by the exponential factor and decays to zero rapidly as the spatial frequency increases in magnitude. $S(\underline{z}_1,\underline{z}_2)$ is quite complex and it's character is determined by the arguments of the exponentials. The character of $S(\underline{z}_1,\underline{z}_2)$ can be best illustrated by example. By using inverse Fourier transforms, the mean $s(\underline{x})$ and covariance $R_s(\underline{x}_1,\underline{x}_2)$ functions of $s(\underline{x})$ can be obtained from $\bar{S}(\underline{z})$ and $S_s(\underline{z}_1\underline{z}_2)$.

Figure 1 shows typical speckle images for astronomical and simulated data. The astronomical data was obtained by S. F. Worden of the Sacramento Peak Observatory. Figure 2 contains average images and the magnitudes of their Fourier transforms which illustrate the low pass nature of the mean of the optical transfer function $\bar{S}(\underline{z})$. Figure 3 shows the broadband nature of the variance of the optical transfer function. For the binary star, the nulls of the image spectrum give the separation and orientation of the stars. Figure 4 contains magnitude and phase pictures of one-step correlations of Fourier transforms of images. The magnitude pictures show the broadband nature of these correlations. The phase picture for the point source reveals the coherent nature of the differential phase. For extended sources, Figures 3 and 4 show that both the magnitude and phase pictures are modified by the source. For the binary star, the magnitude pictures clearly show the modulation due to their separation and the phase picture clearly shows the diffraction limit of the telescope.

Model for the Noise Effects

Although the effects of noise are not readily apparent in Figures 1, 2, and 3, they have considerable impact on the restoration of images.

While the notation indicates the above image fields are instantaneous functions of time, there is some finite exposure (i.e., averaging) time involved in their measurement. We assume that these times are short enough to "freeze" the turbulence effects. In the sequel, we will refer to these time-averaged images as

$$i(\underline{x},T_j) = \int_{T_j - \frac{\Delta T}{2}}^{T_j + \frac{\Delta T}{2}} I_p(\underline{x},t)dt \quad . \tag{5}$$

Telescopic images are generally recorded using either photographic film or electronic cameras, often at limited photon flux levels. When using photographic film, the noise is introduced mainly by the non-linear density versus exposure characteristic and film grain noise. Similarly most electronic cameras have a non-linear transfer chacteristic between the exposing light intensity and their output voltage. Other sensor noise sources are electronic noise, shot noise, uncertainties in the scanner beam profile, etc.

Under various hypotheses, the effect of these noise sources can be modeled using combinations of Poisson, additive, and multiplicative noise terms[9]. For additive noise with zero mean and variance σ_a^2, the measured image $i_d(\underline{x},T_j)$ is given by

$$i_d(\underline{x},T_j) = i(\underline{x},T_j) + n_a(\underline{x},T_j) \quad . \tag{6}$$

For multiplicative noise with unity mean and variance σ_m^2, we have

$$i_d(\underline{x},T_j) = i(\underline{x},T_j)\, n_m(\underline{x},T_j) \quad . \tag{7}$$

For Poisson (photon) noise, we have

$$i_d(\underline{x},T_j) = \frac{1}{P_c} n_p(\underline{x},T_j) \quad . \tag{8}$$

The mean and variance of the Poisson process are given by

$$\bar{n}_p(\underline{x},T_j) = \frac{P_c}{I_o}\, \overline{i(\underline{x})}, \tag{9}$$

and

$$\sigma_p^2(\underline{x}) = \frac{P_c}{I_o}\, \overline{i\,\underline{x}} \quad . \tag{10}$$

where

$$\overline{i(\underline{x})} = E\{i(\underline{x},t)\} \quad , \tag{11}$$

$$I_o = \iint_{-\infty}^{\infty} \overline{i(\underline{x})}\, d\underline{x}, \tag{12}$$

and

$$P_c = \text{total photon flux detected.} \tag{13}$$

In all cases, the noise is statistically independent of $i(\underline{x},T_j)$, and spatially and temporally uncorrelated.

Sample Image Statistics

This section gives the relationships between the sample statistics of a set of images with sensor noise and the mean and covariance of the point spread response.

First, consider the first order statistics or simple average of an ensemble of images. Taking the expected value of (1) gives

$$\overline{i(\underline{x})} = \int_{-\infty}^{\infty} o(\underline{\lambda}) \, \overline{s(\underline{x} - \underline{\lambda})} \, d\underline{\lambda} \tag{14}$$

This integral equation can be solved for the object if a low-noise long exposure image or average of many images is used to approximate $\overline{i(\underline{x})}$. Let the average of N images at times t_j; $j = 1, \ldots N$ be given by

$$\hat{\overline{i(\underline{x})}} = \frac{1}{N} \sum_{j=1}^{N} i(\underline{x}, t_j) \tag{15}$$

For any combination of the Poisson, additive, and multiplicative noise models of (6), (7), and (8), the sample mean is unbiased,

$$E\{\hat{\overline{i(\underline{x})}}\} = \overline{i(\underline{x})} \quad . \tag{16}$$

Unfortunately, these first-order statistics contain very little high-spatial-frequency information because $\overline{s(\cdot)}$ is a wide smooth function with greatly attenuated high spatial frequencies (see Fig. 2). Thus, the solution of (15) results in an enhancement of the measurement noise at high spatial frequencies. The low pass nature of $\overline{s(\cdot)}$ causes the inversion of (14) to be ill-conditioned (small variations in $\overline{i(\underline{x})}$ result in large variations of $o(\underline{x})$).

Now, consider the second order statistics or covariance of an ensemble of images. Taking the covariance of (1) gives

$$R_i(\underline{x}_1, \underline{x}_2) = E\{[i(\underline{x}_1, t) - \overline{i(\underline{x}_1)}] \, [i(\underline{x}_2, t) - \overline{i(\underline{x}_2)}]\}$$

$$= \int_{-\infty}^{\infty}\int_{-\infty}^{\infty} o(\underline{\lambda}_1) o(\underline{\lambda}_2) \, R_s(\underline{x}_1 - \underline{\lambda}_1, \, \underline{x}_2 - \underline{\lambda}_2) \, d\underline{\lambda}_1 d\underline{\lambda}_2 \quad . \tag{17}$$

In this integral equation, the object $o(\underline{\lambda})$ appears as the cartesian product with itself. An unambiguous solution of this non-linear integral equation will require a non-linear solution method. The method will depend on the characteristics of the sample image covariance used in the inversion of (18). Let $\hat{R}_i(\underline{x}_1, \underline{x}_2)$ be the sample covariance function of N images at time $t_j, j = 1, \ldots, N$, then

$$\hat{R}_i(\underline{x}_1, \underline{x}_2) = \frac{1}{N-1} \sum_{j=1}^{N} [i_d(\underline{x}_1, T_j) - \hat{\overline{i(\underline{x}_1)}}] \, [i_d(\underline{x}_2, T_j) - \hat{\overline{i(\underline{x}_2)}}] \tag{18}$$

The sample covariance is unbiased only if there is no measurement noise. For any combination of the Poisson, additive, and multiplicative noise models of (6), (7), and (8), the expected value of the sample covariance is given by

$$E\{\hat{R}_i(\underline{x}_1, \underline{x}_2)\} = R_i(\underline{x}_1, \underline{x}_2) + \delta(\underline{x}_1 - \underline{x}_2) \left[\sigma_a^2 + \sigma_m^2 \, [R_i(\underline{x}_1, \underline{x}_2) + \overline{i(\underline{x}_1)} \; \overline{i(\underline{x}_2)}] + \frac{I_c}{P_o} \overline{i(\underline{x}_1)}\right] \tag{19}$$

Note that the bias depends on the mean and covariance of the image and is zero except where $\underline{x}_1 = \underline{x}_2$. Once these biases are subtracted from the sample covariance, (17) can be solved for the object using the two broadband dimensions of $R_s(\underline{x}_1, \underline{x}_2)$.

Principle Value Decomposition

The kernel of (17) involving the object, $o(\underline{\lambda}_1)o(\underline{\lambda}_2)$ is a four-dimensional function. A general four-dimensional function can be expanded into an infinite sum of two-dimensional cartesian products, (10)

$$f(\underline{x}_1, \underline{x}_2) = \sum_{i=1}^{\infty} E_i \, g_i(\underline{x}_1) \, g_i(\underline{x}_2) \quad . \tag{20}$$

The E_i are the eigenvalues and the $g_i(\underline{x})$ are the eigenfunctions of $f(\underline{x}_1,\underline{x}_2)$. The E_i are ordered by magnitude and the $g_i(\underline{x})$ are orthonormalized. If we attempted to solve (18) for the general four-dimensional kernel, we would have two difficulties. First, the four dimensions would imply the square of the number of operations involved in a two-dimensional problem. Second, (17) is ill-conditioned in two of its dimensions (for $\underline{x}_1=\underline{x}_2$ (17) gives the variance of $i(\underline{x},t)$ which is a slowly varying or narrow band function). If we decomposed the general (4-D) kernel by using (20) and take the principle value $(e_1, g_1(\underline{x}))$, we have (17). Thus, the solution of (17) is given by the largest eigenvalue and its eigenfunction for the corrected sample covariance of the images. Here the norm used is in the sense of integral over the covariance of the point spread function $R_s(\underline{x}_1,\underline{x}_2)$. The typical algorithm used to solve for the largest eigenvalue and its eigenfunction is the "power method."[11] The algorithm in the next section is an adaptation which uses the special properties of $S(\underline{x})$ and $R_s(\underline{x}_1,\underline{x}_2)$ to reduce the amount of computation required.

Reconstruction Algorithm

For the assumed case of isoplanatic or spatially invariant imaging, the convolution nature of (14) and (17) allows us to use the Fourier transform to rewrite (14) and (17)

$$\bar{I}(\underline{z}) = \theta(\underline{z})\bar{S}(\underline{z}) \tag{21}$$

and

$$S_i(\underline{z}_1,\underline{z}_2) = \theta(\underline{z}_1)\theta^*(\underline{z}_2)S_s(\underline{z}_1,\underline{z}_2) \quad . \tag{22}$$

where

$\theta(\underline{z})$ is the transform of the object,

$\bar{I}(\underline{z})$ is the mean of the Fourier transform of the image

$S_i(\underline{z}_1,\underline{z}_2)$ is the covariance of the Fourier transform of the image

$\bar{S}(\underline{z})$ is the mean optical transfer function

$S_s(\underline{z}_1,\underline{z}_2)$ is the covariance of the optical transfer function

Let

$\hat{\bar{I}}(\underline{z})$ be the sample mean of the Fourier transforms of the images

and

$\hat{S}_i(\underline{z}_1,\underline{z}_2)$ be the sample covariance of the Fourier transforms of the images.

The expected values of these are

$$E\{\hat{\bar{I}}(\underline{z})\} = \bar{I}(\underline{z}) \tag{23}$$

and

$$E\{\hat{S}_i(\underline{z}_1,\underline{z}_2)\} = S_i(\underline{z}_1 + \underline{z}_2) + \sigma_a^2\,\delta(\underline{z}_1 - \underline{z}_2) + \frac{I_o}{P_o}[\bar{I}(\underline{z}_1 - \underline{z}_2)] + \sigma_m^2 \int_{-\infty}^{+\infty}\int [\bar{I}(\underline{z}_1 - \underline{\beta})\bar{I}^*(\underline{z}_1 - \underline{\beta}) + S_i(\underline{z}_1 - \underline{\beta}, \underline{z}_2 - \underline{\beta})]\, d\underline{\beta} \tag{24}$$

If the noise model is accurate and the parameters are known, the sample covariance can be corrected for the effects of noise. If not, within the constraints of this or another noise model, the parameters can be estimated and used to correct the sample covariance. Figure 5 summarizes the restoration algorithm. The estimation equations are detailed below.

Given the corrected sample covariance, the "power" method of finding the principle eigenvalue and its eigenfunction can be applied. This consists of picking an initial estimate and forming the appropriate products of it and the sample covariance in a matrix multiplication fashion. Properly normalizing these products gives the next estimate of $\theta(\underline{z})$. As this process is repeated, only the eigenfunction corresponding to the principle (largest) eigenvalue does not decay from the estimate.

Let $\theta^{\ell}(\underline{z})$ be the ℓ-th estimate. Then for a particular value of $\underline{z}$, equations corresponding (21) and (22) are written as

$$\theta^{\ell+1}(\underline{z}_1)\ [\theta^{\ell *}(\underline{z}_2) S_s(\underline{z}_1,\underline{z}_2)] = \hat{S}_o(\underline{z}_1,\underline{z}_2)$$

$$= \hat{S}_i(\underline{z}_1,\underline{z}_2) - \sigma_a^2[\delta(\underline{z}_1 - \underline{z}_2)] - \frac{I_o}{P_o}[\bar{I}(\underline{z}_1 - \underline{z}_2)]$$

$$-\sigma_m^2 \iint_{\infty}^{\infty} [\bar{I}(\underline{z}_1 - \underline{\beta})\bar{I}^*(\underline{z}_2 - \underline{\beta}) + S_i(\underline{z}_i - \underline{\beta}, \underline{z}_2 - \underline{\beta})]d\underline{\beta} \qquad (25)$$

and

$$\theta^{\ell+1}(\underline{z}_1)\ \bar{S}(\underline{*}) = \hat{\bar{I}}(z) \qquad (26)$$

where only values of $\underline{z}_2$ near $\underline{z}_1$ are used, $|\underline{z}_1 - \underline{z}_2| < r_o$. r_o is the correlation distance in the aperture plane resulting from the turbulence[12]. Because the sample statistics are used, these equations have errors. The equations for $|\underline{z}_1 - \underline{z}_2| > r_o$ are dominated by errors and are discarded. The corresponding components of $S_i(\underline{z}_1,\underline{z}_2)$ are not computed, greatly reducing the order of the computation (proportional to N^2 rather than N^4 for N x N images). These equations at a particular value of $\underline{z}$, are solved for $\theta^{\ell+1}(\underline{z}_1)$ in a least square fashion (the "appropriate product") to give

$$\theta^{\ell+1}(\underline{z}_1) = \frac{\sum_{|\underline{z}_2-\underline{z}_1|<r_o} [\theta^{\ell *}(\underline{z}_2) S_s(\underline{z}_1,\underline{z}_2)]\ [\hat{S}_i(\underline{z}_1,\underline{z}_2)] + \alpha \hat{I}(\underline{z}_1)\bar{S}(\underline{z}_1)}{\sum_{|\underline{z}_2-\underline{z}_1|<r_o} \theta^{\ell *}(\underline{z}_2)\ S_s(\underline{z}_1,\underline{z}_2)^2 + \alpha \bar{S}^2(\underline{z}_1)} \qquad (27)$$

where α is a weighting parameter to control the relative importance of the sample mean and sample covariance (α=o for $|\underline{z}_1| > r_o$). These equations are solved for each $\underline{z}_1$ starting at the origin proceeding toward the diffraction limit in a spiraling manner.

The parameters of the noise model are estimated (if desired) after (27) has been applied at all $\underline{z}_1$. The estimate is obtained by a least squares solution of

$$\hat{S}_i(\underline{z}_1,\underline{z}_2) = c_o \theta^{\ell}(\underline{z}_1)\theta^{\ell *}(\underline{z}_2) S_s(\underline{z}_1,\underline{z}_2) + c_1[\delta(\underline{z}_1 - \underline{z}_2)] \qquad (28)$$

$$+ c_2\, B(\underline{z}_1 - \underline{z}_2) + c_3 \hat{\bar{I}}(\underline{z}_1 - \underline{z}_2)$$

for the coefficients c_o, c_1, c_2, and c_3 where $B(\underline{z}_1 - \underline{z}_2)$ is a precalculated approximation to the integral of (25). The coefficients c_1, c_2, c_3 are used as σ_a^2, σ_m^2, and $\frac{I_o}{P_o}$ on the next iteration. The square root of c_o is used to scale $\theta^{\ell}(\underline{z}_1)$ before the next iteration.

Restoration Results

The restoration algorithm has been exercised on both simulated and astronomical data. Figures 6 and 7 show the results which reveal a substantial restoration under a variety of conditions. Simple analytic models were used for $\bar{S}(z)$ and $S_s(\underline{z}_1,\underline{z}_2)$

$$\bar{S}(\underline{z}) \approx \exp\ [-(|\hat{\underline{z}}|/r_o)^2] \qquad (29)$$

and

$$S_s(\underline{z}_1,\underline{z}_2) \approx \left(\frac{r_o}{D}\right)^2 \left[1 - \frac{|\underline{z}_1 + \underline{z}_2|}{2D} - \bar{S}\left(\frac{\underline{z}_1 + \underline{z}_2}{2}\right)\right]\left[\bar{S}\left(\frac{\underline{z}_1 - \underline{z}_2}{2}\right)\right] \qquad (30)$$

A variety of conditions were simulated to obtain a feeling for the sensitivity of the restoration technique. Figure 6A shows the ideal diffraction limited image. Figure 1F shows a typical speckle image. The average image and its spectrum are in Figures 2C and 2D. When no measurement errors are introduced, the restoration is very accurate as shown in Figure 6D. For photon noise corresponding to a magnitude of 0.5, restorations without correcting for the noise bias have an impulsive artifact near the centroid of the image (Figures 6B and 6C). This artifact is removed when the proper bias correction is made to the covariance data (Figures 6E and 6F). The remaining errors are caused by the small number of images used in the sample statistics and the simplified models used to describe $\bar{S}(z)$ and $S_s(z_1,z_2)$. Forty images were used in the restorations of Figures 6C and 6F, and eighty images were used in all other restorations of Figure 6. Figure 6G shows the degradation of the restoration caused by a factor of four reduction in the photon flux. Figures 6H and 6I show the degradation of the restoration caused by estimating the parameters of the noise models for photon noise alone and for all three components. The impulsive artifact returns partially and some high spatial frequency artifacts are introduced. These new artifacts are probably caused by the simplified models for the optical transfer function statistics and the bias errors in the covariance data.

Figure 7 shows the results of restorations of the binary star. A typical speckle image is in Figure 1E. The average image and its spectrum for 44 images are in Figures 2I and 2J. Figure 7A shows the restoration of the binary star where the noise parameters have been estimated. Unfortunately, insufficient information and time were available to independently determine the noise model parameters for this data. The very broad speckle images have been reduced dramatically to an elongated spot in the center of the image field. The magnitude and phase of the Fourier transform of the restoration in Figures 7B and 7C show the coherence of the phase wherever the magnitude is appreciable and that the restoration approaches the diffraction limit. The impulsive artifact at the centroid of the image lies between and over the locations of the individual stars. Figure 7D is a factor of eight enlargement of the restoration. Because the stars are separated by only slightly more than the diffraction limited resolution, the artifact precludes directly resolving them. Figure 7E shows a restoration where the artifact has been removed by estimating it from the previous restoration and a restoration without a correction for the noise bias which has a larger impulsive artifact.

Conclusions

The restoration technique has been demonstrated to be effective with both simulated and astronomical data. Bias corrections to the second order statistics were found to be necessary. The restoration technique converges quickly and its required computational effort is roughly proportional to the size of the images.

References

1. J. W. Sherman, "A Posteriori Restoration of Atmospherically Degraded Images using Multiframe Imagery," in Image Processing, Proceedings of the S.P.I.E. 74, 249-258 (1976).
2. A. Labeyrie, "Attainment of Diffraction Limited Resolution in Large Telescopes by Fourier Analyzing Speckle Patterns in Star Images," Astron. & Astrophys. 6, 85 (1970).
3. K. T. Knox and B. J. Thompson, "Recovery of Images from Atmospherically Degraded Short-Exposure Photographs," Astrophysical J., 193; L 45-L 48, October 1974.
4. R. L. Pante, "Some Results on the Imaging of Incoherent Sources Through Turbulence," J. Opt. Soc. Am. 66, 574 (1976).
5. A. M. Schneiderman and D. P. Kare, "Transfer Functions, Correlation Scales and Phase Retrieval in Speckle Interferometry," J. Opt. Soc. Am. 67, 1583, (1977).
6. P. Nisenson, D. C. Ehn, and R. V. Stachnik, "Astronomical Speckle Imaging," in Imaging Through the Atmosphere, Proceedings of the S.P.I.E. 75, 83-88 (1976).
7. S. P. Worden, C. R. Lynds, and J. W. Harvey, "Reconstructed Images of Alpha Orioni's using Stellar Speckle Interferometry," J. Opt. Soc. Am. 66, 1243 (1976).
8. J. B. Breckinridge, "Obtaining Information through the Atmosphere at the Diffraction Limit of a Large Telescope," J. Opt. Soc. Am. 65, 755 (1975).
9. D. G. Falconer, "Noise and Distortion in Photographic Data Storage," IBM J. Res. Dev., Vol. 14, pp. 475-586, September 1970.
10. F. B. Hilderbrand, Methods of Applied Mathematics, second ed., Englewood Cliffs, N. J.; Prentice Hall, 1965.
11. J. H. Wilkinson, "The Algebraic Eigenvalue Problem," Oxford, England, Clarendon Press, 1965.
12. D. L. Fried, "Optical Resolution Through a Randomly Inhomogeneous Medium for Very Long and Very Short Exposures," J. Opt. Soc. Am. 56, 1372 (1966).

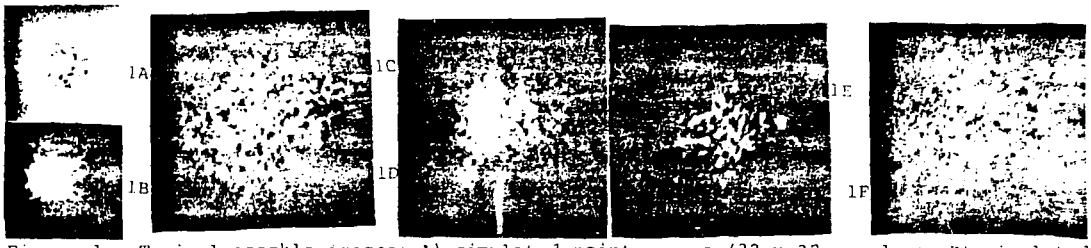

Figure 1. Typical speckle images; A) simulated point source (32 x 32 samples); B) simulated extended source (64 x 64); C) 48 Gem, an unresolved star (128 x 128); D) Vesta, an asteroid (128 x 128); E) Alpha Auriga (Capella), a binary star with an angular separation of ~ 0.06 arc sec. (256 x 256); F) Gamma Orionis (Bellatrix), an unresolved star (256 x 256).

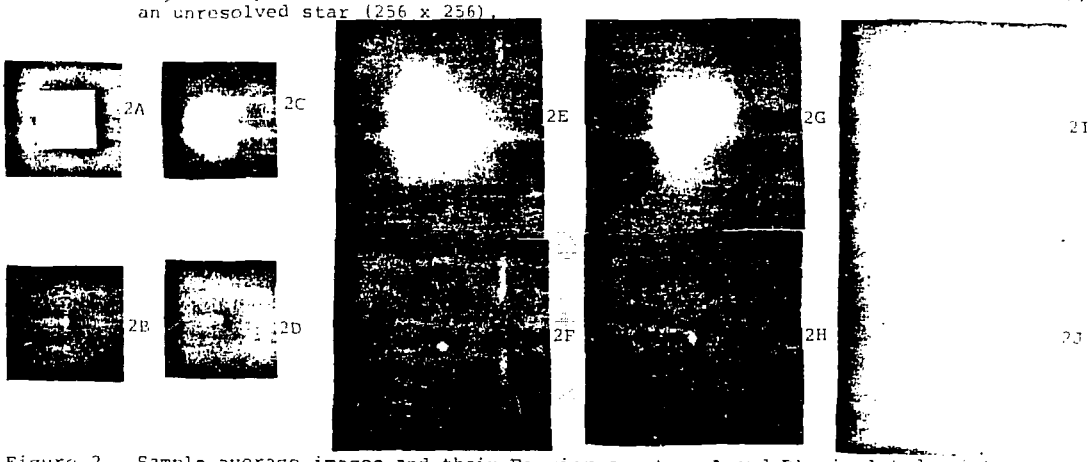

Figure 2. Sample average images and their Fourier spectra; A and B) simulated point source; C and D) simulated extended source; E and F) 48 Gem; G and H) Vesta; I and J) Capella.

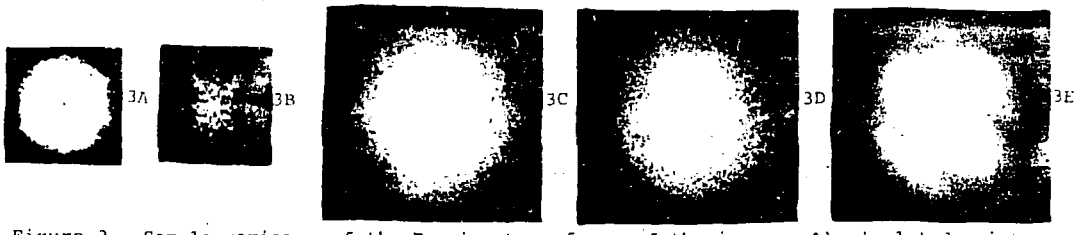

Figure 3. Sample variance of the Fourier transforms of the images; A) simulated point source; B) simulated extended source; C) 48 Gem; D) Vesta; E) Capella.

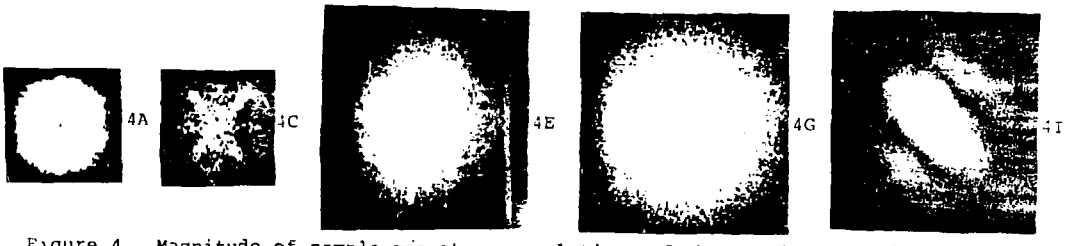

Figure 4. Magnitude of sample one-step correlations of the Fourier transforms of the images; A) simulated point source; C) simulated extended source; E) 48 Gem; G) Vesta; I) Capella.

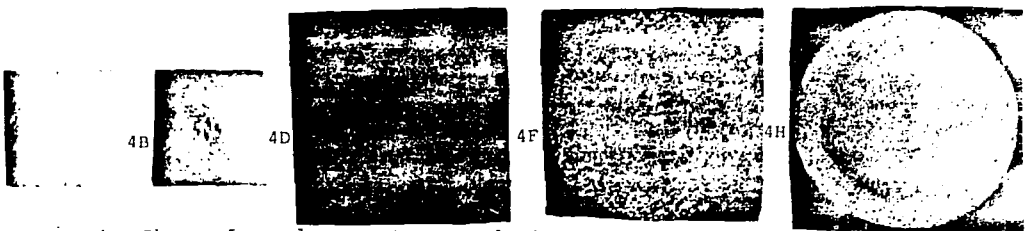

Figure 4. (cont.) Phase of sample one-step correlations of the Fourier transforms of the images: B) simulated point source; D) simulated extended source; F) 48 Gem; H) Vesta; J) Capella.

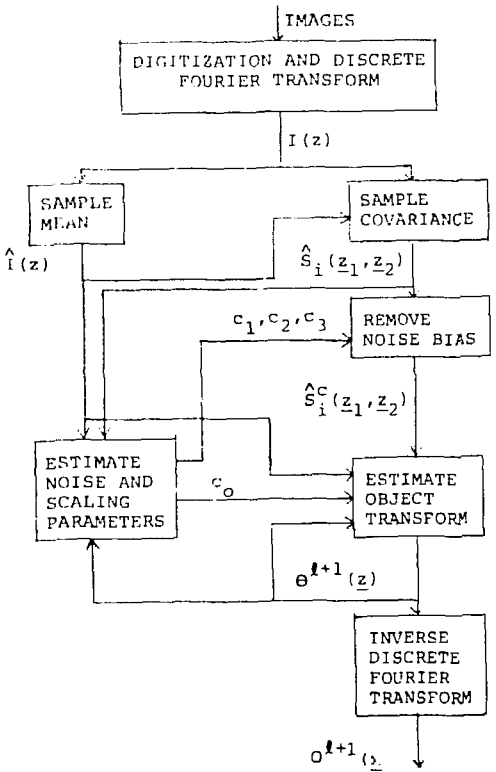

Figure 5. Restoration algorithm block diagram.

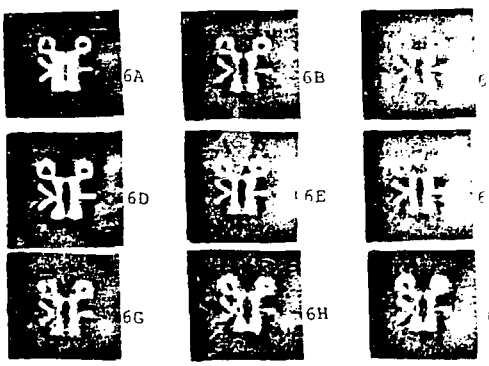

Figure 6. Restorations of simulated data; A) image without atmospheric turbulence or noise; B) no bias correction (80 images); C) no bias correction (40 images); D) no measurement noise (80 images); E) exact bias correction (80 images), F) exact bias correction (40 images); G) exact bias correction with a quarter of photon flux (80 images); H) estimated bias correction for photon noise only (80 images); I) estimated bias correction for all noise components (80 images).

Figure 7. Restoration of Capella; A) restored image for estimated bias correction; B) magnitude of Fourier transform of restored image; C) phase of Fourier transform of restored image magnified (8 times); E) restored image with impulsive artifact reduced.